Journal of Energy Chemistry 54 (2021) 626–638

Contents lists available at ScienceDirect

Journal of Energy Chemistry

journal homepage: www.elsevier.com/locate/jechem

http://www.journals.elsevier.com/journal-of-energy-chemistry/

In situ construction of Co/N/C-based heterojunction on biomass-derived hierarchical porous carbon with stable active sites using a Co-N protective strategy for high-efficiency ORR, OER and HER trifunctional electrocatalysts

Xuehui Lv [1], Zuoxu Xiao [1], Haoyuan Wang, Xinlong Wang, Lulu Shan, Fuling Wang, Chuangyu Wei, Xiangjie Tang, Yanli Chen *

College of Science, School of Materials Science and Engineering, China University of Petroleum (East China), Qingdao 266580, Shandong, China

ARTICLE INFO

Article history:
Received 5 April 2020
Revised 11 June 2020
Accepted 17 June 2020
Available online 24 June 2020

Keywords:
Anisotype heterojunction
Isotype heterojunction
Multifunctional catalyst
Biomass-derived
Prophyrin

ABSTRACT

The facile designs and fabrication of noble metal-free electrocatalysts are highly required to achieve multifunctional catalytic activity with excellent stability in Zn-air batteries, fuel cells and water splitting systems. Herein, a heterostructure engineering is applied to construct the high performance Co, N-containing carbon-based multifunctional electrocatalysts with the feature of isotype (*i.e. n-n* type $Co_2N_{0.67}$-BHPC) and anisotype (*i.e. p-n* type Co_2O_3-BHPC) heterojunctions for ORR, OER and HER. The *n-n* type $Co_2N_{0.67}$-BHPC, in which biomass (*e.g.* mushroom)-derived hierarchical porous carbon (BHPC) incorporated with nonstoichiometric active species $Co_2N_{0.67}$, is fabricated by using an *in situ* protective strategy of macrocyclic central Co-N_4 from CoTPP (5,10,15,20-tetrakis(phenyl) porphyrinato cobalt) precursor through the intermolecular π-π interactions between CoTPP and its metal-free analogue H_2TPP. Meanwhile, an unprotected strategy of macrocyclic central Co-N_4 from CoTPP can afford the anisotype Co_2O_3-BHPC *p-n* heterojunction. The as-prepared *n-n* type $Co_2N_{0.67}$-BHPC heterojunction exhibited a higher density of Co-based active sites with outstanding stability and more efficient charge transfer at the isotype heterojunction interface in comparison with *p-n* type Co_2O_3-BHPC heterojunction. Consequently, for ORR, $Co_2N_{0.67}$-BHPC exhibits the more positive onset and half-wave potentials of 0.93 and 0.86 V vs. RHE, respectively, superior to those of the commercial 20 wt% Pt/C and most of Co-based catalysts reported so far. To drive a current density of 10 mA cm^{-2}, $Co_2N_{0.67}$-BHPC also shows the lower overpotentials of 0.34 and 0.21 V vs. RHE for OER and HER, respectively. Furthermore, the Zn-air battery equipped with $Co_2N_{0.67}$-BHPC displays higher maximum power density (109 mW cm^{-2}) and charge–discharge cycle stability. Interestingly, the anisotype heterojunction Co_2O_3-BHPC as trifunctional electrocatalyst reveals evidently photoelectrochemical enhancement compared with the photostable $Co_2N_{0.67}$-BHPC. That is to say, isotype heterojunction material (*n-n* type $Co_2N_{0.67}$-BHPC) is equipped with better electrocatalytic performance than anisotype one (*p-n* type Co_2O_3-BHPC), but the opposite is true in photoelectrochemical catalysis. Meanwhile, the possible mechanism is proposed based on the energy band structures of the $Co_2N_{0.67}$-BHPC and Co_2O_3-BHPC and the cocatalyst effects. The present work provides much more possibilities to tune the electrocatalytic and photoelectrochemical properties of catalysts through a facile combination of heterostructure engineering protocol and macrocyclic central metal protective strategy.

1. Introduction

Green and renewable energy storage and conversion techniques (such as fuel cells, metal-air batteries and electrochemical water splitting systems) have been targeted as an urgent need with respect to sustainable development of human society to replace

* Corresponding author.
E-mail address: yanlichen@upc.edu.cn (Y. Chen).
[1] These authors contributed equally to this work.

https://doi.org/10.1016/j.jechem.2020.06.040

the traditional techniques [1]. In general, four-electron oxygen reduction and evolution reaction (ORR and OER) are at the heart of the aforementioned systems, while their sluggish kinetics finally limit the practical utilizations compared with two-electron hydrogen evolution reaction (HER) [2]. Up to now, noble metals (*e.g.* Pt, Ir or Ru) still serve as the state-of-the-art benchmark catalysts among these reactions. Nevertheless, prohibitive costs, limited reserves and poor tolerance severely hinder their scalable applications. And it is almost impossible for the single precious metals to possess multifunctional activity of ORR, OER, HER simultaneously. Therefore, unflagging efforts have been devoted to fabricating the precious-metal-free embedded and/or heteroatom (N, P, S or B etc.) doped carbon materials, which can provide remarkably multifunctional electrocatalytic performance and durability alternatives to noble metal based materials to meet the requirements of commercialization [3].

In recent years, more attentions lie in suitable charge transfer modification of carbon-based electrocatalysts achieved by heterojunctions, heteroatom doping, defect engineering, etc., resulting significant improvement in electrocatalytic performance finally [4]. Since individual ingredients exist in composite materials possessing the different electron structures, designing of heterojunction structure is an efficient method to modulate the electrocatalytic performance by modifying the electron structure of the materials. Many pioneer works manifested that heterostructures composed by carbon materials loaded with transition metal compounds represent significantly enhanced electrocatalytic activity due to charge transfer and followed redistribution of electrons stemming from strong coupling effect between different components [5]. On the other hand, when it comes to practical application issues, the stability of catalyst materials as also a critical factor has to be considered in designing the catalyst [6]. Especially, for most of non-noble metal-based catalysts, although the real fuel cell equipped with these catalysts possesses high initial performance, their catalytic activity usually degrade quickly during the operation process. It has been found that the fastest degradation course of catalysts can occur in the first few to 20 h of operation, which accounts for most proportion of overall degradation [7]. Therefore, researchers have delved into the several possible degradation mechanisms aiming for designing more durably and effectively electrocatalysts [8]. The most commonly accepted reasons for degradation are so-called demetalation and carbon oxidation during the reaction process [7,8]. However, very little protocol has put forward to improve the stability of electrocatalysts. Furthermore, the diverse electrocatalytic reactions usually differ in reactive sites and various catalytic steps. Therefore, it is very challenging to achieve high-efficiency multifunctional catalytic activity on a single catalyst with the feature of stability as well as durability. Up to now, more and more attentions focus on transition metal nitrides (TMNs) among the non-noble metal-based catalysts, not only due to their characteristics of high conductivity and stability, but also superior activity for ORR [9], OER [10] and HER [11]. For instance, Lee et al. prepared the Fe_xN/N-CNT-GR catalyst for ORR by using two-step heat treatment, which is consist of iron nitride nanoparticles loaded on carbon nanotube-graphene (CNT-GR) hybrid support [9]. Fe_xN/N-CNT-GR presents superior ORR performance and durability against carbon corrosion and metal dissolution owe to the design of the CNT-GR hybrid support. Kou and co-workers have developed *in situ* coupling cobalt nitride (CoN_x) nanoparticles approach within nitrogen-doped graphene aerogel (NGA) to obtain an efficient trifunctional electrocatalyst (CoN_x/NGA), which is exhibit excellent catalytic performance mainly thanks to the tailored electronic properties originated from the amorphous CoN_x nanoparticles [10]. The great majority of literature reports that the manner of preparing transition metal nitrides basically uses annealing in hazardous ammonia atmosphere [12], meanwhile, the resulting materials do not simultaneously equipped with the peculiarity both superior multifunctional catalytic activity and outstanding stability. Xu and co-workers have developed a facile one-step self-assembly and confined pyrolysis approach to obtain a heterostructural electrocatalysts (Co_2P-CoN-in-NCNTs) with N-doped carbon nanotubes (CNT) encapsulated Co_2P-CoN double active center for HER, OER and ORR [13]. On one hand, distinct electronic structures endow outstanding catalytic activities of transition-metal nitrides. In addition, they found that the strong coupling effect between Co_2P/CoN core/shell and nitrogen doping and graphitic CNTs can significantly boost the electrical conductivity and electrocatalytic activity. Therefore, it is intensely desire to come up with a simple and versatile way to fabricate the heterojunction materials with strong interaction between heterogeneous components, ultimately achieve one electrocatalyst with superior multi-activity and stability simultaneously.

From the perspective of utilizing renewable energy (*e.g.* solar, wind, geothermal), solar-driven photoelectrochemical (PEC) catalysis opens another promising pathway to achieve the purpose of reducing energy consumption and enhancing the electrocatalytic performance. Considering that visible light plays a pivotal role in solar spectrum, pursuing an electrocatalyst with harvesting visible light sufficiently is a highly desired matter. Interestingly, the formation of heterointerfaces can also facilitate the transfer of photoinduced charges by modulating the energy band structure and followed improve PEC catalytic efficiency. In 2018, Dai et al. have raised a new concept of photo-responsive bifunctional ORR/OER electrocatalyst ($Ni_{12}P_5$@NCNT) fabricated by a p-n heterojunction for the first time [14]. They found that the intimate contacts between n-type NCNT and p-type $Ni_{12}P_5$ NPs can promote separate and transfer of photoinduced electrons and holes, further enhancing the electrocatalytic performance of the heterojunction material. This study opens an avenue for novel energy conversion system combined photochemical and electrochemical technology.

Mushroom is a renewable biomass resource widely distributed around the world, available all year round and cheaply obtained. Especially, annual production of edible mushrooms has exceeded 30 million tons by 2019 in China. The moisture content of mushrooms is considerably high, accounting for about 90%, indicating that there are plenty of vascular structure for nutrient uptake and transport [15]. With the help of activator, this type of material is easy to obtain the hierarchically porous structure, which is more facilitated to the diffusion of reactants and electrolytes, and exposure of active sites [15]. In addition, it is well known that heteroatom doping plays a vital role in improving catalytic performance during the preparation of the catalyst, especially the codoped carbon catalysts with synergistic effect [16]. Furthermore, *in situ* self-doping of heteroatoms existed in biomass precursors naturally is far more effective than post-treatment of heteroatom-rich source [17]. As for mushroom, it offers the advantage of N and P sources, as proved by previous literature and work [17]. And based on all the above considerations, in this work, isotype heterojunction catalyst ($Co_2N_{0.67}$-BHPC) are prepared by one-pot co-pyrolysis method after *in-situ* protection of metalloporphyrin (5,10,15,20-tetrakis(phenyl) porphyrinato cobalt, CoTPP). Meanwhile, for comparative purposes, similar preparation method but unprotected strategy for metalloporphyrin (CoTPP) used to fabricate the anisotype heterojunction material (Co_2O_3-BHPC). The electrocatalytic properties of two materials were studied carefully and systematically for ORR, OER and HER under normal and light irradiation conditions. Since the metal at the center of the porphyrin is easily combined with decomposed oxygen element in biomass during the calcination process, the metal-free tetraphenylporphyrin (5,10,15,20-tetraphenylporphyrin, H_2TPP) is used to self-assemble with the CoTPP through the π-π interaction of similar

macrocyclic compounds, to provide protection for center metal Co of CoTPP and decrease the formation of unstable metal oxide. Steady cobalt nitride ($Co_2N_{0.67}$) serves as the main active center in $Co_2N_{0.67}$-BHPC, while the active species of Co_2O_3-BHPC are mainly cobalt oxides owing to implementation of unprotected way. In contrast, $Co_2N_{0.67}$-BHPC exhibits the best performance for ORR, OER and HER with the onset and half-wave potential of 0.93 and 0.86 V vs. RHE for ORR, the overpotentials of 0.34 and 0.21 V vs. RHE for OER and HER, respectively. $Co_2N_{0.67}$-BHPC also shows superior stability compared with Co_2O_3-BHPC. Impressively, Zn-air batteries equipped with $Co_2N_{0.67}$-BHPC achieved higher maximum power density (109 mW cm^{-2}) and charge–discharge cycle stability, surpassing most reported carbon materials. Moreover, under the light irradiation, $Co_2N_{0.67}$-BHPC possesses high photostability, while Co_2O_3-BHPC with p-n heterojunction is able to reduce the electron-hole recombination effectively, facilitate the transfer of interfacial charge and ultimately improve the performance of ORR, OER and HER. Based on the above results, the suitable energy band structures of catalysts and cocatalysts effects are further investigated in details to comprehend the possible mechanism.

2. Experimental

2.1. Chemical and reagents

5,10,15,20-tetraphenylporphyrin (H_2TPP) and 5,10,15,20-tetrakis(phenyl) porphyrinato cobalt (II) (CoTPP) were synthesized according to the protocol described in reference and previously reported article [18]. All other chemical reagents are commercially available and are used directly without further purification. 20 wt% Pt/C and 5 wt% Nafion were purchased from Alfa Aesar Co. Ltd. Ultrapure water was obtained from purification instrument. Mushroom (MR) was purchased from supermarket.

2.2. Preparation of the resultant electrocatalysts

The commercially available MR were cut into small pieces and ground to powder by ball-milling. The powder was subsequently washed with water, ethanol and completely dried at 120 °C in a vacuum drying oven for 24 h. Afterward, the H_2TPP and porphyrinato cobalt (CoTPP) were dissolved in dichloromethane (DCM) and stirred for 3 h (denoted as H_2TPP_1/CoTPP, The subscript number 1 represent the optimal molar ratio of H_2TPP to CoTPP, experimental optimization see Supplementary Materials, Fig. S1), and then added to the totally dried MR powder with a mass ratio of 5:1 (MR: H_2TPP_1/CoTPP). The mixture was adequately stirred at room temperature for 5 h, and then the MR adsorbed with the H_2TPP_1/CoTPP compounds was collected by solvent evaporation under reduced pressure (denoted as MR- H_2TPP_1/CoTPP). MR-H_2TPP_1/CoTPP and $ZnCl_2$ with an optimal mass ratio of 1:3 are mixed and ground for 10 min, and then the mixture is pyrolyzed at 900 °C for 2 h (the heating rate of 5 °C min^{-1}, $ZnCl_2$ dosage and optimization of pyrolysis temperature see Figs. S2 and S3) under flowing nitrogen atmosphere to afford the target product, denoted as $Co_2N_{0.67}$-BHPC (as shown in Scheme 1). For comparison, the MR adsorbed with only CoTPP compound was also prepared under the similar condition, but without involving H_2TPP, and the resultant sample was denoted as Co_2O_3-BHPC (as shown in Scheme 1). In addition, the pure MR powder is pyrolyzed under the optimum temperature to obtain biomass-derived carbon (BC). The mixture of pure MR powder and $ZnCl_2$ is calcined under the optimal conditions without any porphyrin precursors, denoted resultant as BHPC.

3. Results and discussion

3.1. Characterization

The scanning electron microscopy (SEM) image shows that the surface morphology and microstructure of un-calcined MR powder and as-prepared $Co_2N_{0.67}$-BHPC, Co_2O_3-BHPC and BC materials. As depicted in Fig. 1(a–d), the catalyst $Co_2N_{0.67}$-BHPC exhibits a highly porous spongy-like structure compared with a lamellar structure of BC (Fig. S4) prepared from the calcination of pure MR powder (Fig. S4), while the porous structure is hardly visible on the BC layers. As shown in Fig. S5(a–d), abundant nanoparticles appeared on the surface of lamellar structure with the some nanoscale holes are observed for Co_2O_3-BHPC. Obviously, the introduction of porphyrin precursors and activation agent $ZnCl_2$ during the carbonization process make the surface of the pristine stratified structure rougher for both $Co_2N_{0.67}$-BHPC and Co_2O_3-BHPC than that of BC (Fig. S4). The average layer thickness of $Co_2N_{0.67}$-BHPC is ca. 15 μm, which is about 3 times the layer-thickness of BC. Moreover, smaller granular structure was observed for $Co_2N_{0.67}$-BHPC (Fig. 1c) than Co_2O_3-BHPC (Fig. S5) after the carbon layer becomes fluffy. This is more advantageous for efficient exposure of active sites, resulting in its excellent electrocatalytic performance (*vide infra*). The energy dispersive X-ray (EDX) spectrum confirmed the successful doping of Co and N elements into both $Co_2N_{0.67}$-BHPC (Fig. S6) and Co_2O_3-BHPC (Fig. S7). In the meantime, to further research the distribution of those elements in carbon supports, the element mapping diagrams were investigate (Fig. 1e–i and Fig. S5e–i). As clearly seen that Co, C, N and O elements are uniformly distributed throughout the framework (Fig. 1e–h and Fig. S5e–h). In addition, the self-doped P elements from original MR powder are also well distributed homogeneously in both $Co_2N_{0.67}$-BHPC (Fig. 1i) and Co_2O_3-BHPC (Fig. S5i). Carbon framework doped with heteroatoms has been demonstrated to enhance the electrocatalytic performance owing to the enhanced asymmetric electronic structure [1,19]. This is also considered to be one of the reasons why $Co_2N_{0.67}$-BHPC possesses the outstanding electrocatalytic activity (*vide infra*).

Fig. 2 shows the transmission electron microscope (TEM) and high-resolution TEM (HRTEM) images of as-fabricated $Co_2N_{0.67}$-BHPC and Co_2O_3-BHPC. It is worth mentioning that nanometer-sized pores distributed homogeneously were observed in Fig. 2(a) for $Co_2N_{0.67}$-BHPC, in accordance with the SEM images, indicating the successful generating of abundant hierarchical porous architecture with the departure of Zn during the pyrolysis process. HRTEM images (Fig. 2b and c) of $Co_2N_{0.67}$-BHPC found that there are three well-defined crystalline lattice fringes, which possess the *d*-spacing of 0.209, 0.283 and 0.341 nm, corresponding to the (101) plane of $Co_2N_{0.67}$ [20], (200) plane of C_3N_4 [21], and (002) plane of graphitic carbon (GC) [22], respectively. These results mean the successful embedding of Co, N-containing active species in graphitic carbon matrix, developing of heterostructure and ultimately as active centers to enhance the catalytic performance. In addition, the TEM image of Co_2O_3-BHPC (Fig. 2d) suggested that many crystalline particles formed in carbon matrix after calcination, in line with its SEM results. The HRTEM diagrams (Fig. 2e and f) of Co_2O_3-BHPC further exhibited that this carbon-based material is mainly composed of three kinds of phase, and two of them (i.e. C_3N_4 and GC) are identical with $Co_2N_{0.67}$-BHPC, in addition to the formation of the Co_2O_3 phase with a *d*-spacing of 0.291 nm, according with the (002) plane of Co_2O_3 [23].

The powder X-ray diffraction (PXRD) patterns were carried out to further analyze the composition and phase of the as-prepared samples, Fig. 3(a). The PXRD patterns of two types of samples also showed a broad diffraction peak at about 26.4°, which correspond

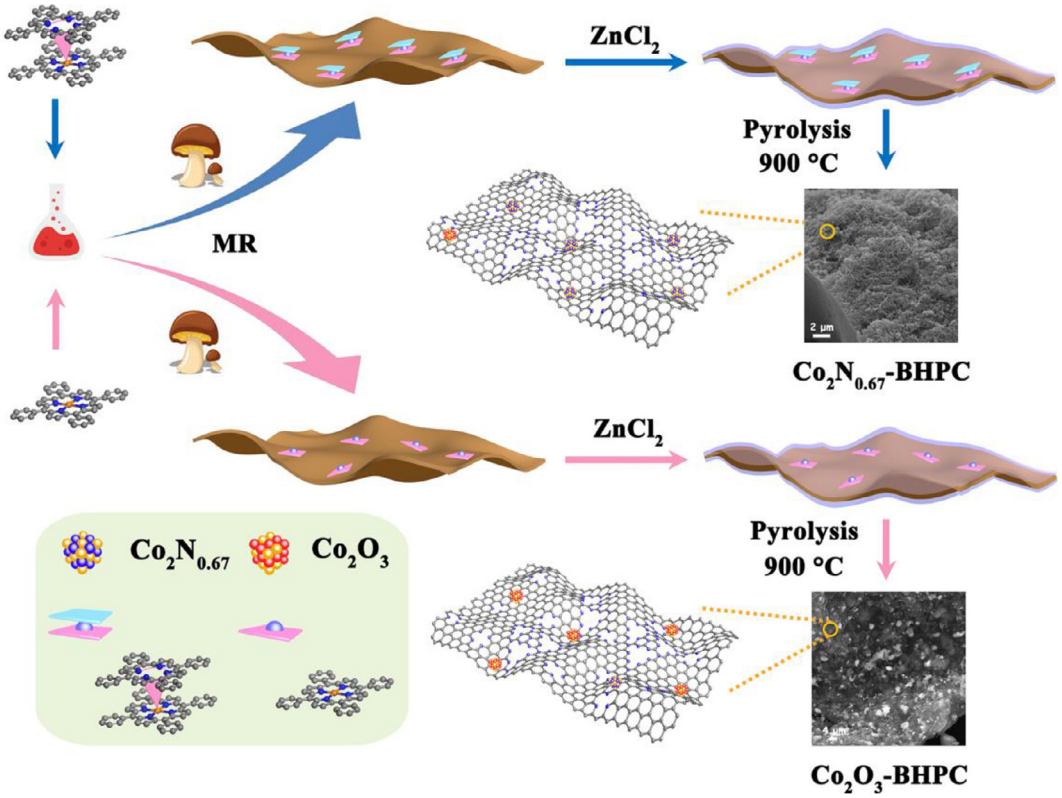

Scheme 1. Steps for synthesis of $Co_2N_{0.67}$-BHPC and Co_2O_3-BHPC.

to the (002) plane of GC phase, disclosing the characteristic structure of amorphous carbon [22]. In $Co_2N_{0.67}$-BHPC, the diffraction peaks at around 41.6° and 44.4° were ascribed to the (002) and (101) planes of $Co_2N_{0.67}$ (PDF#06-0691) [20]. By contrast, the higher and sharper diffraction peaks located at *ca.* 31.1° and 38.6° were present in Co_2O_3-BHPC, which are well indexed to the (002) and (102) plane of Co_2O_3 (PDF#02-0770), implying that large amount of metal cobalt forms the Co_2O_3 phase derived from the Co-N_4 macrocycle and MR precursors [23]. Note that the weak diffraction peak located at 44.4° can be assigned to the (101) plane of $Co_2N_{0.67}$ (PDF#06-0691) phase for Co_2O_3-BHPC, indicating that a small amount of $Co_2N_{0.67}$ is also generated in addition to the abundant Co_2O_3 in Co_2O_3-BHPC. These results implied that cobalt detached from the Co-N_4 macrocycle is more easily combined with the oxygen decomposed in biomass during the high-temperature treatment in the absence protection of the metal-free porphyrin (H_2TPP). On the other hand, no obvious diffraction peaks of Co_2O_3 are observed for $Co_2N_{0.67}$-BHPC, verifying that this protection strategy (that enables Co-N fixed at the center of the CoTPP macrocycle hard to be replaced by Co-O under the protection of H_2TPP) is available. In addition, the phase of C_3N_4 (PDF#50–1512) are also detected in both of as-obtained materials [21].

Nitrogen adsorption/desorption isotherm in Fig. 3(b) exhibited that both of samples possess the hierarchical porous feature, which present a typical hysteresis type curves with the steep adsorption at both low and high relative pressure sides. This result indicates that micropores, mesopores and macropores appear in both of as-prepared carbons [24]. The use of the same activator $ZnCl_2$ endows very similar specific surface area for both $Co_2N_{0.67}$-BHPC and Co_2O_3-BHPC. The Brunauer-Emmett-Teller (BET) specific surface area was estimated to be 648.7 $m^2\ g^{-1}$ and 634.4 $m^2\ g^{-1}$ in terms of $Co_2N_{0.67}$-BHPC and Co_2O_3-BHPC, respectively (Fig. 3b). However, the pore size distribution curves of two materials revealed a higher average pore size of ca. 4.7 nm for $Co_2N_{0.67}$-BHPC than ca. 2.6 nm for Co_2O_3-BHPC (see inset of Fig. 3b). This indicated that $Co_2N_{0.67}$-BHPC possesses favorable pore size, which is expected to more facilitate the transport of both aqueous electrolyte ions and gaseous species than Co_2O_3-BHPC [25]. It is worth noting that the difference of the distinctively total pore volume was observed to be ca. 0.958 $cm^3\ g^{-1}$ for $Co_2N_{0.67}$-BHPC and 0.441 $cm^3\ g^{-1}$ for Co_2O_3-BHPC (Table S1, Supplementary Materials), respectively. Especially, $Co_2N_{0.67}$-BHPC exhibits the highest mesopore volume ratio of 93.8% as compared to 67.3% for Co_2O_3-BHPC (Table S1). Such a large mesopore volume ratio in $Co_2N_{0.67}$-BHPC can enhance the utilization of active sites $Co_2N_{0.67}$ by forming channels to otherwise untouchable sites [26]. All of these factors are expected to yield beneficial catalytic properties (*vide infra*).

In general, abundant porous structure is accompanied with the generation of defected carbon structures in quantity. Therefore, in order to investigate the differences of the disorder level and graphitic characteristics among the as-fabricated samples, the Raman spectrum was further performed as shown in Fig. 3(c). The $Co_2N_{0.67}$-BHPC has three typical Raman bands, which are indexed to the sp^3 defect sites (D band, 1336 cm^{-1}), E_{2g} vibrational mode of sp^2-bonded pairs (G band, 1590 cm^{-1}) and 2D band (2814 cm^{-1}) from graphite layers. In terms of Co_2O_3-BHPC, the same the D and G bands from graphite layers as those in $Co_2N_{0.67}$-BHPC are also observed, meanwhile the additional peaks located between 400 and 700 cm^{-1} are found which are assigned to the vibration mode of Co-O [27]. This result also suggested the generation of Co_2O_3 specie, in well agreement with the results of HRTEM and PXRD. Furthermore, the intensity ratio (I_D/I_G) of D band to G band is 1.06 and 1.00 for $Co_2N_{0.67}$-BHPC and Co_2O_3-BHPC, respectively, which suggests the more graphitic edge and topological defects exist in $Co_2N_{0.67}$-BHPC relative to Co_2O_3-BHPC after pyrolysis. Both porous and defected structure for $Co_2N_{0.67}$-BHPC

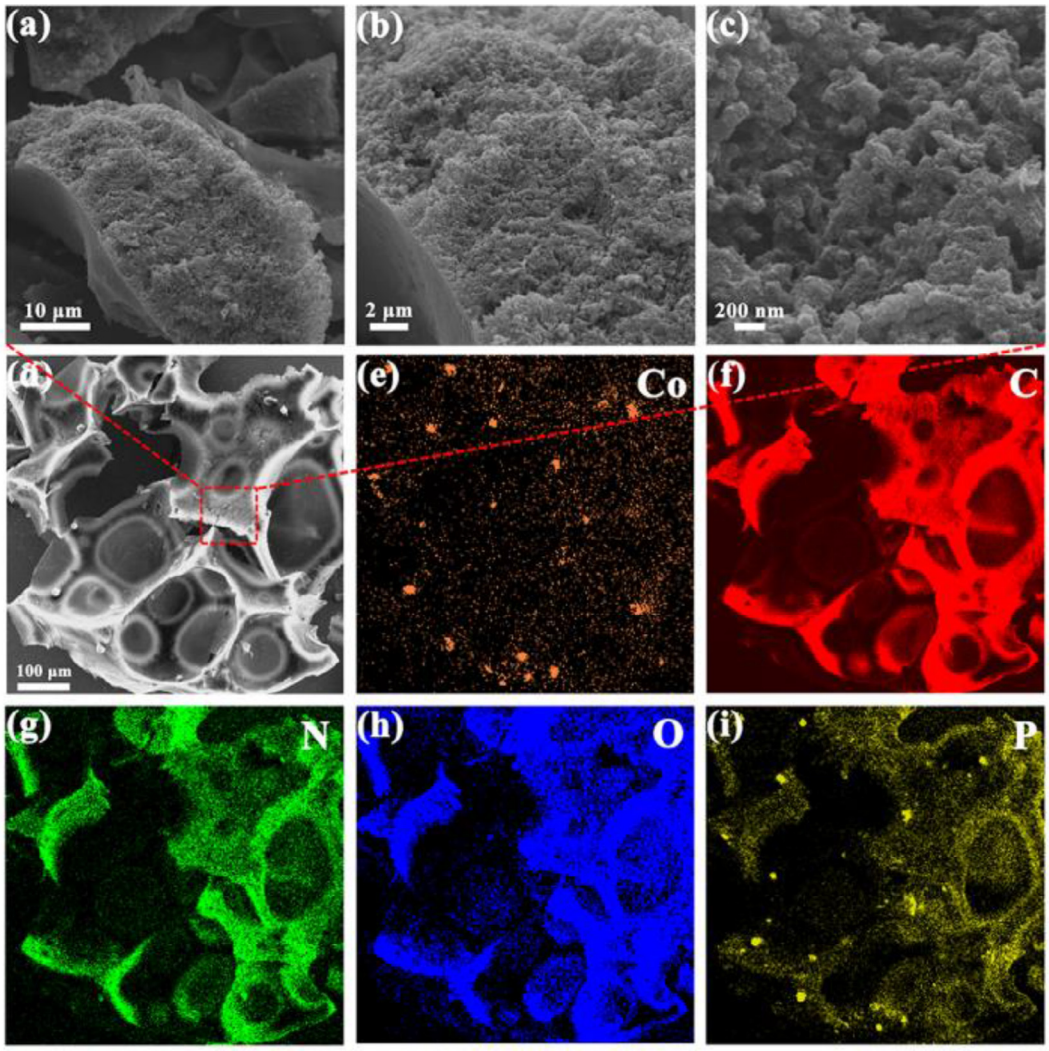

Fig. 1. (a–d) SEM images, (e–i) elemental mapping diagrams of $Co_2N_{0.67}$-BHPC.

are more beneficial to the exposure of active sites, O_2 adsorption and subsequently favorable for rapid charge/mass transport [28].

X-ray photoelectron spectroscopy (XPS) was carried out to ascertain the chemical statuses and bonding configurations of the elements and further confirm the existence of catalytic active sites. Fig. 3(d) and Fig. S8 show the XPS survey of the $Co_2N_{0.67}$-BHPC and Co_2O_3-BHPC. As expected, both of them attested to the existence of the characteristic spectra of Co, C, N, O and P with the surface element contents of 1.23, 83.04, 2.73, 12.06 and 0.94 at% for $Co_2N_{0.67}$-BHPC and 0.84, 82.34, 1.47, 14.66 and 0.69 at% for Co_2O_3-BHPC, respectively. Note that the surface contents of Co (1.23 at%), and N (2.73 at%) in $Co_2N_{0.67}$-BHPC are much higher than those (Co, 0.84 at% and N, 1.47 at%) of Co_2O_3-BHPC, which should be attributed to the present of H_2TPP in H_2TPP/CoTPP precursor. In the meantime, inductively coupled plasma optical emission spectrometer (ICP-OES) measurement and elemental analysis (EA) were performed with the view of gaining the content of Co and N in bulk catalysts of $Co_2N_{0.67}$-BHPC and Co_2O_3-BHPC. As can be seen Table S2, the higher contents of Co and N in $Co_2N_{0.67}$-BHPC (1.34 and 3.02 wt%) than in Co_2O_3-BHPC (0.99 and 1.75 wt%) were revealed. This is agreement with the surface contents of Co and N in two samples, attesting the uniform distribution of element on surface and bulk phase for both of them. Consequently, this manifests that the present Co-N_4 protective strategy by using intermolecular π-π interactions between H_2TPP and CoTPP is available for effective loading Co and N elements into the bio-carbon material.

The high resolution Co 2*p* XPS spectrum of catalyst $Co_2N_{0.67}$-BHPC is presented in Fig. 3(e) and can be classified into three doublets corresponding to Co^{3+} (779.8 and 795.8 eV), Co^{2+} (781.8 and 797.5 eV) and satellite peaks (785.1 and 802.5 eV) [29]. The features of three doublets are also true for Co_2O_3-BHPC with the same binding energy, as shown in Fig. S9. Meanwhile, as shown in N 1*s* spectrum of $Co_2N_{0.67}$-BHPC (Fig. 3f), there shows four deconvoluted sub-peaks located at about 398.2, 400.6, 401.8 and 399.4 eV, respectively, which are attributed to the pyridinic-N (content: 38 at%), pyrrolic-N (18 at%), graphitic-N (27 at%) and Co-N (17 at%) (Table S3) [30]. This, combined with the results of HRTEM and PXRD mentioned above, unambiguously confirmed the formation of the Co-N bonding in $Co_2N_{0.67}$-BHPC. Furthermore, the electron-accepting pyridinic-N and graphitic-N, the sum of their proportions (65 at%) occupy the dominant percentage of N configurations in $Co_2N_{0.67}$-BHPC (shown in Fig. 3f). As a consequence, the surface properties and electronic structure of the carbon-based catalysts can be efficiently modified by the formation of pyridinic-N and graphitic-N in the carbon matrix [31]. This is beneficial to boost the reaction kinetics of the ORR, OER and HER owing to generated positive charge around the sp^2-hybridized car-

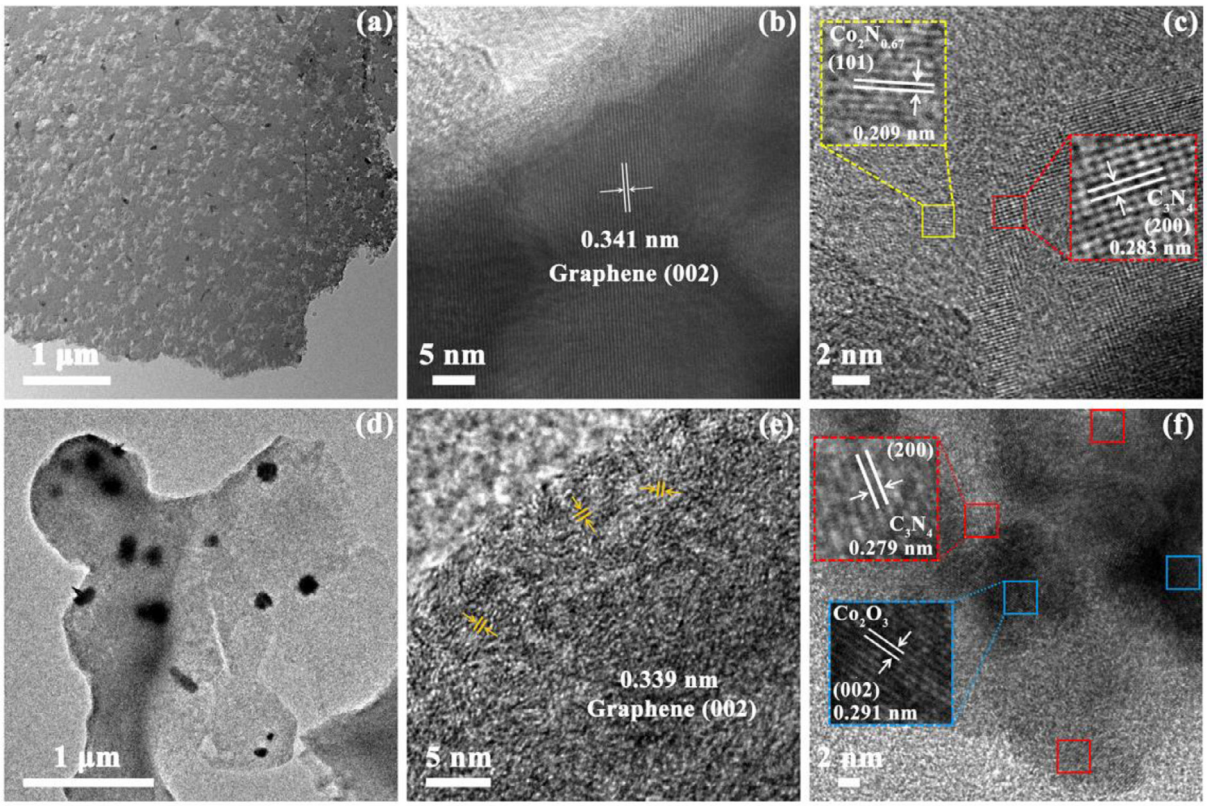

Fig. 2. (a) TEM image, (b and c) HRTEM images of $Co_2N_{0.67}$-BHPC; inset in (c): the lattice fringe images. (d) TEM image, (e and f) HRTEM images of Co_2O_3-BHPC; inset in (f): the lattice fringe images.

bon atoms originated from both of N types [29,32]. As for Co_2O_3-BHPC, the N 1*s* spectrum also displays four types of N configuration with the relative contents of 5, 43, 49 and 4 at% for pyridinic-N, pyrrolic-N, graphitic-N and Co-N, respectively, Fig. 3(g). In contrast, the total content of pyridinic-N and graphitic-N accounts for only 54 at%, which is much less than 65 at% of $Co_2N_{0.67}$-BHPC. Furthermore, the N atom bonded with Co covalently (4 at% Co-N) also illustrates trace amounts of cobalt nitride generated in Co_2O_3-BHPC during the calcination process. The O 1*s* core-level spectrum of $Co_2N_{0.67}$-BHPC is given in Fig. 3(h), which can be deconvoluted into three typical components at 531.1, 532.1 and 533.6 eV, respectively, corresponding to C=O/oxygen vacancies, C-OH/C-O-C and C-O/O-P with the relative contents of 10, 58 and 33 at% (Table S3) [33]. Unlike $Co_2N_{0.67}$-BHPC having no detectable Co-O band, in O 1*s* spectrum of Co_2O_3-BHPC (Fig. 3i), four subpeaks are split, involving the lattice O (O^{2-}) of the Co-O band at 530.4 eV (7 at%) in addition to the C = O/oxygen vacancies at 531.7 eV (16 at%), the C-OH/C-O-C at 532.4 eV (15 at%) and the C-O/O-P at 533.6 eV (62 at%) (Table S3). It is well known the formation of oxygen vacancies can act as additional active edge sites to promote the adsorption of adsorbent molecules from the perspective of surface defects strategies and to further boost the electrocatalytic activity [34]. Moreover, abundant oxygen vacancies are equipped with the ability to trap the electron and/or hole, thereby suppressing the photogenerated charge carriers recombination efficiently in terms of energy band structure [35]. This further facilitates the photoelectrochemical response of multifunctional catalysis for Co_2O_3-BHPC (*vide infra*). The high-resolution P 2*p* signal disclose the nature of self-doped P element exist in as-prepared materials, Figs. S10 and S11. The peak was fitted into two parts at about 131.1 and 133.4 eV, assigned to P-C and P-O species for two carbons [33]. The self-doped P atom is believed to beneficial for catalytic activity [36]. It is worth noting that Co_2O_3-BHPC exhibits less contents of pyridinic-N and Co-N compared with those in $Co_2N_{0.67}$-BHPC in spite of the same four types of N configuration (i.e. pyridinic-N, pyrrolic-N, graphitic-N and Co-N) in the N 1*s* spectra of two materials (as shown in Table S3). This in turn demonstrated the availability of protected strategy of the macrocyclic central Co-N_4 for the resulting $Co_2N_{0.67}$-BHPC catalyst. It seems also true for the O 1*s* spectra of two materials with the higher contents of C-OH/C-O-C relative to C-O/O-P in cobalt nitrides dominated catalyst of $Co_2N_{0.67}$-BHPC. The similar phenomena for O 1*s* XPS spectra in cobalt nitrides dominated catalyst have been founded in our previous report [18]. As seen from Figs. S12 and S13, the fitted peaks for high-resolution C 1*s* of $Co_2N_{0.67}$-BHPC and Co_2O_3-BHPC centered at about 284.2, 284.6, 285.2, 286.0, 287.2 and 290.4 eV are attributed to sp^2 C, sp^3 C, C-N, C-O/C-P, C=O/C-O-C and π–π^*, respectively [37]. The presence of C-N peak indicated that the N atom is incorporated into the skeleton of carbon successfully. This concurs exactly with the results of HRTEM and PXRD. Furthermore, the higher content of sp^3 C component (24 at%) than that of sp^2 C component (18 at%) unravels that more disordered structure of carbon exist in $Co_2N_{0.67}$-BHPC than those of (sp^3 C = 12 at%, sp^2 C = 36 at%) Co_2O_3-BHPC, which is in accordance with the above results.

3.2. Electrochemical characterization

To evaluate the electrocatalytic activity of $Co_2N_{0.67}$-BHPC and Co_2O_3-BHPC toward the ORR, the cyclic voltammetry (CV) curves were first measured in N_2– or O_2-saturated 0.1 M KOH electrolyte (Fig. S14). It was found that two as-prepared catalysts deliver featureless CV curves in N_2-saturated electrolyte while the most positive reduction peak potential around at 0.86 V was present in $Co_2N_{0.67}$-BHPC than that of Co_2O_3-BHPC (0.82 V) in O_2-saturated

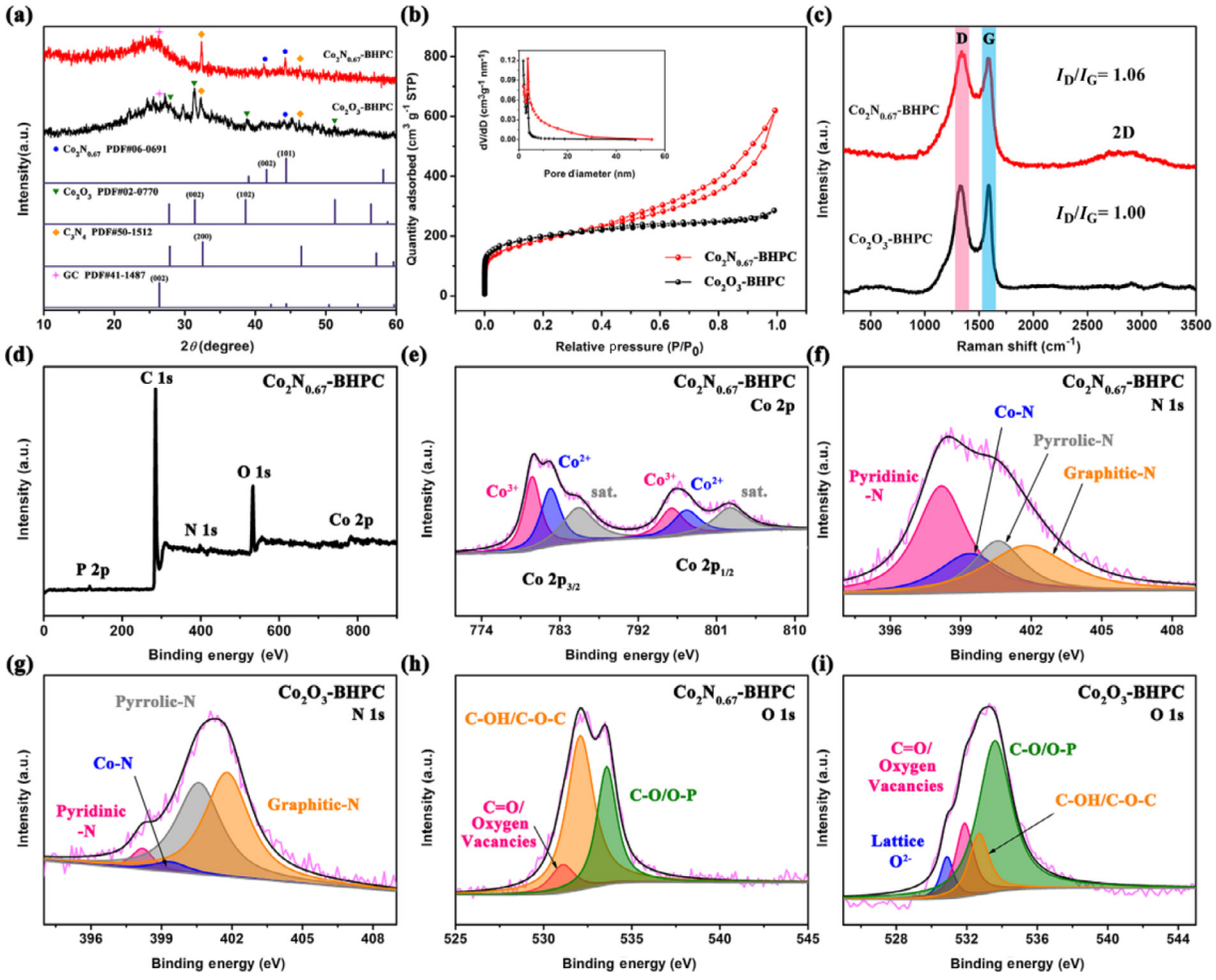

Fig. 3. (a) PXRD patterns, (b) nitrogen adsorption–desorption isotherms and pore size distribution (the inset) and (c) Raman spectra of the as-prepared $Co_2N_{0.67}$-BHPC and Co_2O_3-BHPC. (d) The wide XPS survey spectrum of $Co_2N_{0.67}$-BHPC. High-resolution XPS spectra of (e) Co 2*p*, (f) N 1*s*, (h) O 1*s* for $Co_2N_{0.67}$-BHPC and (g) N 1*s*, (i) O 1*s* for Co_2O_3-BHPC, respectively.

solution, suggesting a higher catalytic activity of $Co_2N_{0.67}$-BHPC. The linear scan voltammogram (LSV) curves in Fig. 4(a) further confirm the high intrinsic ORR catalytic activity of $Co_2N_{0.67}$-BHPC. A most positive onset (E_{onset}) and half-wave potential ($E_{1/2}$) of 0.93 and 0.86 V, as well as larger diffusion-limited current density (J_L = 5.68 mA cm^{-2}) were observed in $Co_2N_{0.67}$-BHPC compared with Co_2O_3-BHPC (E_{onset} = 0.89 V; $E_{1/2}$ = 0.82 V, J_L = 4.24 mA cm^{-2}, Fig. 4a). These catalytic performance indexes of $Co_2N_{0.67}$-BHPC were also superior to that of the 20 wt% Pt/C and most of Co-based catalysts (Fig. 4a and Table S4) reported so far. Furthermore, the $Co_2N_{0.67}$-BHPC exhibits a smaller Tafel slope of 47 mV dec^{-1} than Co_2O_3-BHPC (61 mV dec^{-1}) (Fig. 4b), implying that $Co_2N_{0.67}$-BHPC possesses the faster electron transfer rate.

The remarkable catalytic performance of $Co_2N_{0.67}$-BHPC may be due to the following factors. First of all, the transition metal nitrides (cobalt nitrides) possess the excellent electrical conductivities and stability as reported previously [11,38]. It can also act as an electron acceptor, receiving electrons from the N-doped carbon. Next, the charge transfer at the interface between $Co_2N_{0.67}$ and N-doped carbon containing the phase of C_3N_4 in $Co_2N_{0.67}$-BHPC heterojunction can trigger redistribution of electrons, especially around the defect sites, leading to more effective electronic modulation for the catalyst. Ultimately, large specific surface area, optimal pore size, efficiently exposed active sites, moderate defect together with the above all jointly boost the electrocatalytic performance.

Electrochemical impedance spectroscopy (EIS) also further testified the faster charge transfer ability of $Co_2N_{0.67}$-BHPC with the smaller semicircular diameter in Nyquist plots than Co_2O_3-BHPC (Fig. S15). To evaluated the ORR pathways for as-obtained catalysts, on the one hand, the electron transfer number (n) was calculated by the Koutecky-Levich (K-L) curves derived from the LSV plots at various rotation speeds (Fig. 4(c) and Fig. S16). The K-L curves present excellent linearity and near parallelism from 0.3 to 0.7 V. Meanwhile, the n were determined to be ~4.0 and 3.8 for $Co_2N_{0.67}$-BHPC and Co_2O_3-BHPC, disclosing that an apparent four-electron oxygen reduction process for both of carbons. On the other hand, the rotation ring-disk electrode (RRDE) measurements were further carried out. As depicted in Fig. S17, the average n obtained from RRDE measurements was also 4.0 and 3.8 for $Co_2N_{0.67}$-BHPC and Co_2O_3-BHPC, respectively, concordant with the calculated results from K-L plots. Furthermore, only a small amount of H_2O_2 was generated for $Co_2N_{0.67}$-BHPC (less than 2%) over a potential range from 0.2 to 0.8 V versus RHE, while the Co_2O_3-BHPC produced more H_2O_2 (less than 11%). This result indicating that the ORR process catalyzed by $Co_2N_{0.67}$-BHPC more inclined to a four-electron transfer pathway. Fig. S18 shows the CV curves at the non-Faradic region used to assess the electrochemical surface area (ECSA). The exposure degree of active sites can be judged by the value of electrical double-layer capacitance (C_{dl}) due to the linearly proportional between C_{dl} and ECSA. The C_{dl} values of $Co_2N_{0.67}$-BHPC and Co_2O_3-BHPC are 8.34 and 5.67

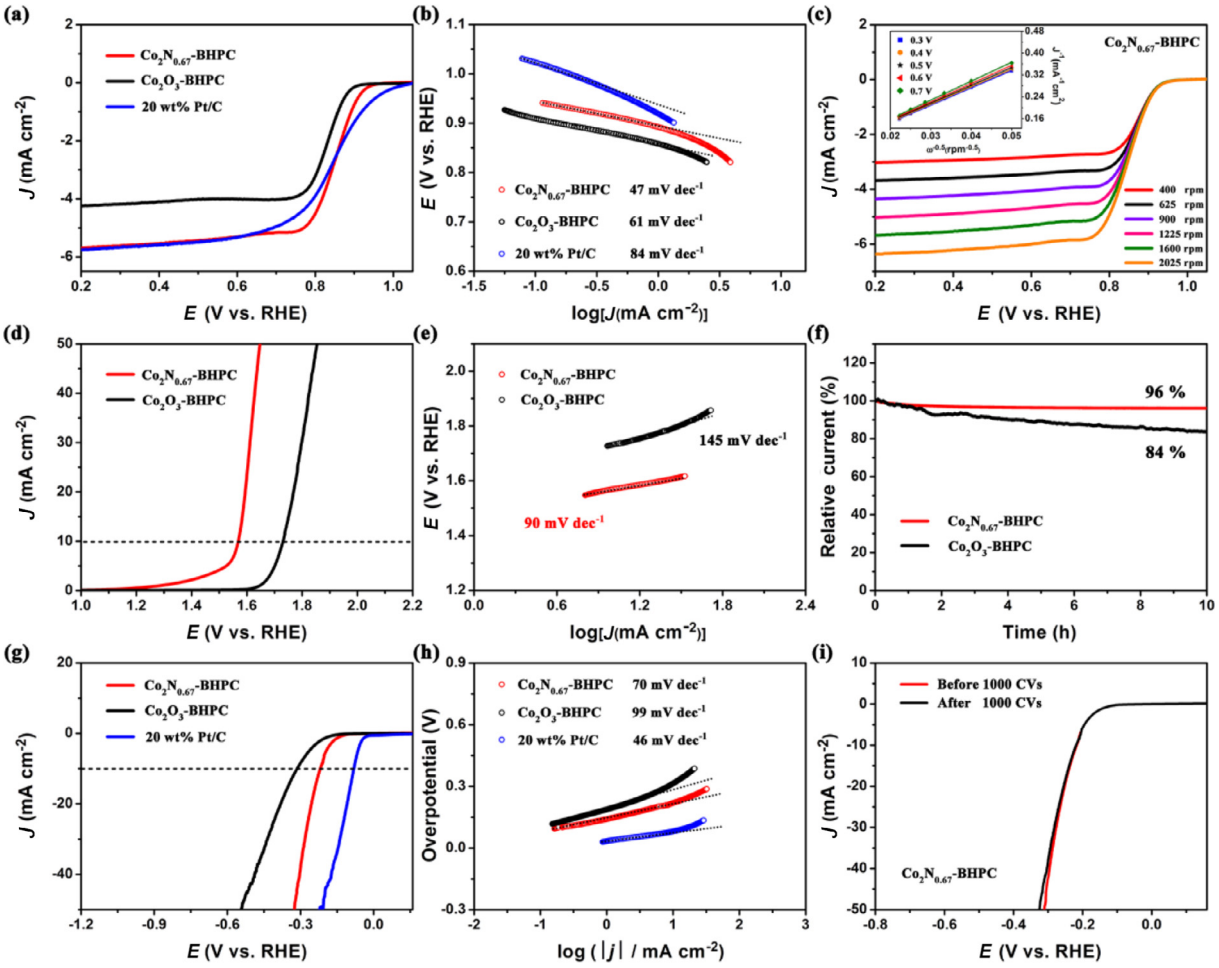

Fig. 4. The ORR, OER, and HER performance of $Co_2N_{0.67}$-BHPC, Co_2O_3-BHPC and 20 wt% Pt/C. (a) ORR LSV curves at a rotation rate of 1600 rpm and (b) ORR Tafel plots of various catalysts in O_2-saturated 0.1 M KOH. (c) LSV curves of $Co_2N_{0.67}$-BHPC at various rotating speeds; inset in (c): K-L plots for $Co_2N_{0.67}$-BHPC at various potentials. (d) LSV curves, (e) derived Tafel plots and (f) chronoamperometric responses for the OER of $Co_2N_{0.67}$-BHPC and Co_2O_3-BHPC in 1 M KOH. (g) HER polarization curves and (h) derived Tafel plots of various catalysts in 1 M KOH. (i) HER LSV curves recorded for $Co_2N_{0.67}$-BHPC before and after 1000 CV cycles.

mF cm^{-2}, respectively, illustrating that much more exposed surface reactive sites present in $Co_2N_{0.67}$-BHPC. This makes it possible to increase the catalytic activity [39]. This result may be caused by the larger mesopore volume ratio of $Co_2N_{0.67}$-BHPC obtained from N_2 adsorption/desorption curves, which is more facilitate the exposure of active sites [26]. In addition, the excellent long-term stability and immunity toward methanol of $Co_2N_{0.67}$-BHPC was verified by chronoamperometry measurements. After a continuous operation time of 10 h, the $Co_2N_{0.67}$-BHPC preserves about 94% of its original current density in 0.1 M KOH, while it is about 81% for Co_2O_3-BHPC (Fig. S19). They are all superior to 20 wt% Pt/C electrode. In addition, Fig. S20 shows the accelerated durability tests of $Co_2N_{0.67}$-BHPC catalyst. There is no obvious variation in terms of $E_{1/2}$ (only negative shift 2 mV after 5000 cycles) and J_L, further indicating the superb durability of $Co_2N_{0.67}$-BHPC even superior than numerous transition metal nitride-based catalysts (see Table S5). $Co_2N_{0.67}$-BHPC electrode also exhibited super immunity to methanol crossover after the injection of 3 M methanol compared with Co_2O_3-BHPC and 20 wt% Pt/C (Fig. S21). All these results clearly illustrated that $Co_2N_{0.67}$-BHPC possesses salient ORR catalytic activity and strong stability.

Meantime, to evaluate the multifunctional activities of as-prepared $Co_2N_{0.67}$-BHPC and Co_2O_3-BHPC, the performance of OER and HER are further investigated in O_2-saturated and N_2-saturated 1.0 M KOH electrolyte. As shown in Fig. 4(d), similar to the case for the ORR, the $Co_2N_{0.67}$-BHPC reveals higher OER activity, which affords a lower overpotential of 0.34 V at a current density of 10 mA cm^{-2} than that of Co_2O_3-BHPC (0.50 V). Moreover, the Tafel slope was calculated by fitting the polarization curves of $Co_2N_{0.67}$-BHPC and Co_2O_3-BHPC to assess their OER kinetics, Fig. 4(e). A smaller Tafel slope can be observed for $Co_2N_{0.67}$-BHPC (90 mV dec^{-1}) relative to the Co_2O_3-BHPC (145 mV dec^{-1}). These results are comparable or superior to those of the reported multifunctional electrocatalysts (Table S6). The satisfactory OER stability of as-synthesized $Co_2N_{0.67}$-BHPC is given in Fig. 4(f). $Co_2N_{0.67}$-BHPC keeps high stability with about 96% current retention after 10 h. By contrast, the Co_2O_3-BHPC only retained about 84% under the same conditions. This indicated that the $Co_2N_{0.67}$-BHPC also possess the preeminent durability for OER in alkaline medium.

As regards the HER catalytic activity in 1.0 M KOH electrolyte, Fig. 4(g) displays the polarization curves of $Co_2N_{0.67}$-BHPC, Co_2O_3-BHPC and 20 wt% Pt/C. Obviously, $Co_2N_{0.67}$-BHPC shows the significantly enhanced performance compared to Co_2O_3-BHPC. To drive a current density of 10 mA cm^{-2}, an overpotential of only 0.21 V is required for the $Co_2N_{0.67}$-BHPC, lower than Co_2O_3-BHPC (0.32 V). Also, the Tafel slope of the catalysts being regarded as one of the great tools to speculate the rate determining step of HER process [40]. As shown in Fig. 4(h), the Tafel slopes of 70 and 99 mV dec^{-1} were achieved for $Co_2N_{0.67}$-BHPC and Co_2O_3-BHPC, respectively, suggesting that the HER kinetics of two as-

prepared samples was determined by a Volmer-Heyrovsky combination mechanism [41]. Meanwhile, these results illustrated that the HER catalytic ability of $Co_2N_{0.67}$-BHPC is still much better than Co_2O_3-BHPC and superior to the reported Co-based catalysts in alkaline solution (Table S7). To assess the durability of $Co_2N_{0.67}$-BHPC in HER, the polarization curve was carried out after continuous 1000 CV cycles and shown in Fig. 4(i). As observed, these two LSV curves almost overlap before and after 1000 CV cycles for $Co_2N_{0.67}$-BHPC in base medium, disclosing the outstanding stability and practical application perspective of $Co_2N_{0.67}$-BHPC.

In order to testify the effect of the other components that are not contained in mushrooms, we have been added a set of control experiments of the BHPC prepared by mushroom powder and $ZnCl_2$ without any porphyrin precursors. The electrocatalytic properties of BHPC were investigated under the same condition as $Co_2N_{0.67}$-BHPC and Co_2O_3-BHPC, Figs. S22–S24. As can be seen, BHPC exhibited very poor catalytic performance for ORR, OER and HER, which in turn further confirmed the positive impact of the other components (i.e. CoTPP and H_2TPP) in as-prepared catalysts on boosting electrocatalytic activity.

3.3. Performance of Zn-air batteries

Considering the prominent ORR performance of as-prepared $Co_2N_{0.67}$-BHPC, the performance of $Co_2N_{0.67}$-BHPC, Co_2O_3-BHPC and Pt/C as the cathode catalysts was evaluated in a Zn-air battery. For comparison purpose, the Co_2O_3-BHPC and commercial Pt/C electrodes were also tested under the same condition. As depicted in Fig. 5(a), the equipped $Co_2N_{0.67}$-BHPC battery shows a higher open circuit voltage of 1.526 V than Co_2O_3-BHPC (1.334 V) and commercial Pt/C (1.420 V), and remains almost unchanged after 15000 s. Moreover, the battery assembled from $Co_2N_{0.67}$-BHPC exhibits a maximum power density of *ca.* 109 mW cm^{-2} at a current density of 176 mA cm^{-2} according to the polarization and power density curves (Fig. 5b), superior to Co_2O_3-BHPC (~52 mW cm^{-2} at 69 mA cm^{-2}), Pt/C (~78 mW cm^{-2} at 119 mA cm^{-2}) and numerous reported batteries based on carbons (Table S8). Fig. 5(c) exhibits the discharge and charge polarization curves of the Zn-air battery with $Co_2N_{0.67}$-BHPC electrode. The Zn-air battery equipped with $Co_2N_{0.67}$-BHPC is also very durable, it maintains a high voltage with almost no voltage decay by using the galvanostatic discharge tests (Fig. 5d). When being galvanostatically discharged at a current density of 5 and 10 mA cm^{-2} again for 2 h, the cell voltage of Zn-air battery with $Co_2N_{0.67}$-BHPC electrode can be restored to its initial level, but not the case for Co_2O_3-BHPC. The Zn-air battery equipped with Co_2O_3-BHPC electrode reveals more low voltage and remarkable attenuation in the galvanostatic discharge plots (see Fig. 5d). Furthermore, mechanical recharging tests were performed by replenishing the spent anode and electrolyte, as shown in Fig. 5(e), the cell voltage plateaus are almost the same after three cycles at 10 mA cm^{-2} for $Co_2N_{0.67}$-BHPC cathode electrode. Such characteristics further highlighting the excellent rate capability and robust nature of $Co_2N_{0.67}$-BHPC. Furthermore, the battery with the $Co_2N_{0.67}$-BHPC air electrode was used to power a commercial light emitting diode (1.5 V) (Fig. 5f), confirming the significant potential of as-fabricated $Co_2N_{0.67}$-BHPC material. Finally, to further assess the stability of two carbons, the cycling performance of the $Co_2N_{0.67}$-BHPC and Co_2O_3-BHPC based Zn-air batteries were recorded employing galvanostatic discharging and charging at 10 mA cm^{-2} for a total about 105 h, as seen in Fig. 5(g). A negligible voltage change can be found in Zn-air batteries with $Co_2N_{0.67}$-BHPC electrode compared with Co_2O_3-BHPC, revealing superior long-term durability of $Co_2N_{0.67}$-BHPC. The above results demonstrate that $Co_2N_{0.67}$-BHPC can be applied in real Zn-air batteries as alternative to commercial Pt/C catalyst.

3.4. Photo-responsive electrocatalytic activity investigation

To unveil the semiconductors types of the $Co_2N_{0.67}$-BHPC and Co_2O_3-BHPC, Mott-Schottky measurements were performed, as shown in Fig. 6(a and b). $Co_2N_{0.67}$-BHPC exhibits the feature of n-type semiconductors with a positive slope in Mott-Schottky plot (Fig. 6a) [42]. It also can be observed that the Mott-Schottky curve of Co_2O_3-BHPC (Fig. 6b) presents an inverted "V-shape", indicating p-n heterojunction formed in Co_2O_3-BHPC [43]. These results illustrate that isotype and anisotype heterojunction were formed in two materials, respectively, due to C_3N_4-doped carbon served as one n-type semiconductor [44]. Meanwhile, the photocurrent density as a valid test means can obtain the information of charge carrier separation efficiency. Fig. 6(c) shows the transient photocurrent measurements of as-prepared samples. Two materials can produce an improvement in photocurrent density upon the visible light irradiation, manifesting that they can both generated the electrons and holes under irradiation. In contrast, Co_2O_3-BHPC displays the significantly increased photocurrent intensity of about 1.32 μA cm^{-2}, which is 5 times that of $Co_2N_{0.67}$-BHPC (0.25 μA cm^{-2}), demonstrating that Co_2O_3-BHPC with p-n heterojunction can effective reduce the electron-hole recombination and facilitate the transfer of interfacial charge upon irradiation. As the isotype heterojunction possess photostable, next, only the Co_2O_3-BHPC was performed photo-responsive multifunctional electrochemical analysis by measuring the photocurrent density-potential curves under chopped light illumination and LSV curves upon the visible light irradiation. As shown in Fig. 6(d–f), the Co_2O_3-BHPC exhibits a typical ON-OFF photocurrent response in current density vs. potential curves. Moreover, under the visible light irradiation, three electrocatalytic performance of Co_2O_3-BHPC have been significantly improved (Figs. S25–S27). It can be seen that the ORR performance of Co_2O_3-BHPC drastically enhanced upon irradiation especially in diffusion-limited current density and half-wave potential ranges of 4.24–4.72 mA cm^{-2} and 0.82–0.84 V, respectively (Fig. S25). As expected, the photo-assisted performances of OER and HER are also improved. The overpotentials at current density of 10 mA cm^{-2} were significantly reduced from 0.50 to 0.45 V and 0.32 to 0.29 V in OER and HER process, respectively, as seen in Figs. S26 and S27. These conclusions indicated that the Co_2O_3-BHPC with anisotype heterojunction can be used as an effective photo-responsive multifunctional catalyst, and the $Co_2N_{0.67}$-BHPC with isotype heterojunction is an effective photostable multifunctional catalyst, and ultimately both can be used in energy conversion systems.

3.5. Mechanism of photoelectrochemical response and stabilization

To get in-depth understanding to the these behaviors of electrocatalytic reaction under light induction, the optical property and energy band structure of two materials were investigate by using valance band (VB) XPS spectra and UV–vis diffuse reflectance spectra (DRS). Meanwhile, the possible mechanism was elucidated for the photoelectrochemical response and stabilization. The VB-XPS plots afford the VB maximum (VBM) edge of materials, as shown in Figs. S28 and S29 [45]. Consequently, the main VB position is located at around 1.48 and 1.59 eV for $Co_2N_{0.67}$-BHPC and Co_2O_3-BHPC, respectively. Notably, the distinct band tail at 0.40 V was found in VB-XPS curve of Co_2O_3-BHPC, which is absent in $Co_2N_{0.67}$-BHPC, due to the more oxygen vacancies exist in Co_2O_3-BHPC than that in $Co_2N_{0.67}$-BHPC, as mentioned from the results of XPS O 1*s* spectrum [35]. VBM of Co_2O_3-BHPC gradually lowered until blue-shifted to 0.40 eV, which generates a large amount of mid-gap states above the VBM, and eventually comes into being a continuum band [46], that is, band tail states (composed exactly by this continuum band together with the VB) [47]. Meanwhile, the

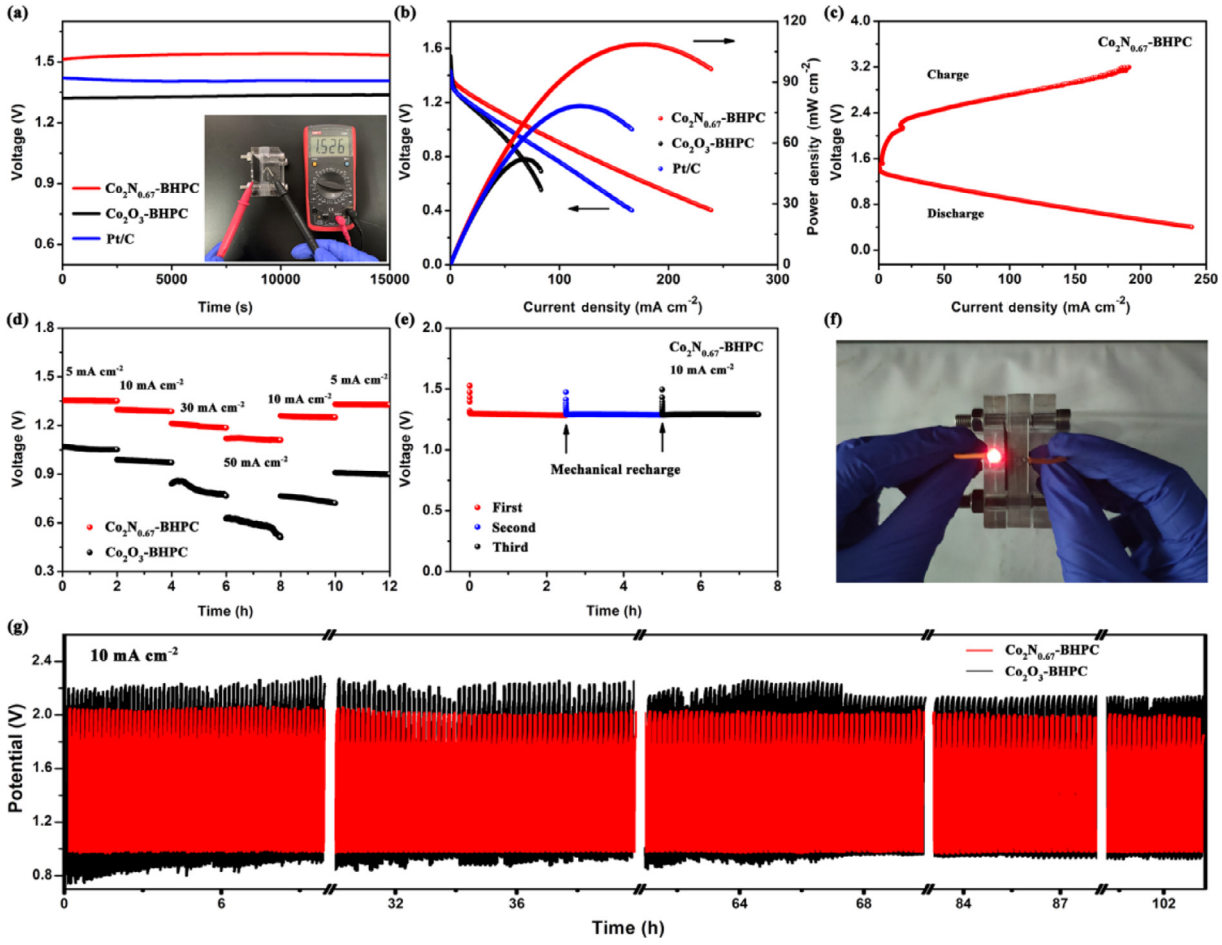

Fig. 5. (a) Open circuit voltage plots of various catalysts; inset in (a): photograph of the Zn-air battery equipped with $Co_2N_{0.67}$-BHPC with an open-circuit voltage of 1.526 V. (b) Discharge polarization curves and power densities of the batteries. (c) Charge and discharge polarization profiles of $Co_2N_{0.67}$-BHPC. (d) Galvanostatic discharge curves of batteries equipped with $Co_2N_{0.67}$-BHPC and Co_2O_3-BHPC. (e) Durability of the battery using $Co_2N_{0.67}$-BHPC catalyst at a current density of 10 mA cm^{-2}, the battery is mechanically rechargeable. (f) Optical images of a red LED (1.5 V) powered by one battery with $Co_2N_{0.67}$-BHPC powder. (g) Galvanostatic charge–discharge profile of the Zn-air battery equipped with $Co_2N_{0.67}$-BHPC and Co_2O_3-BHPC at a current density of 10 mA cm^{-2} with 5 min discharge and 5 min charge.

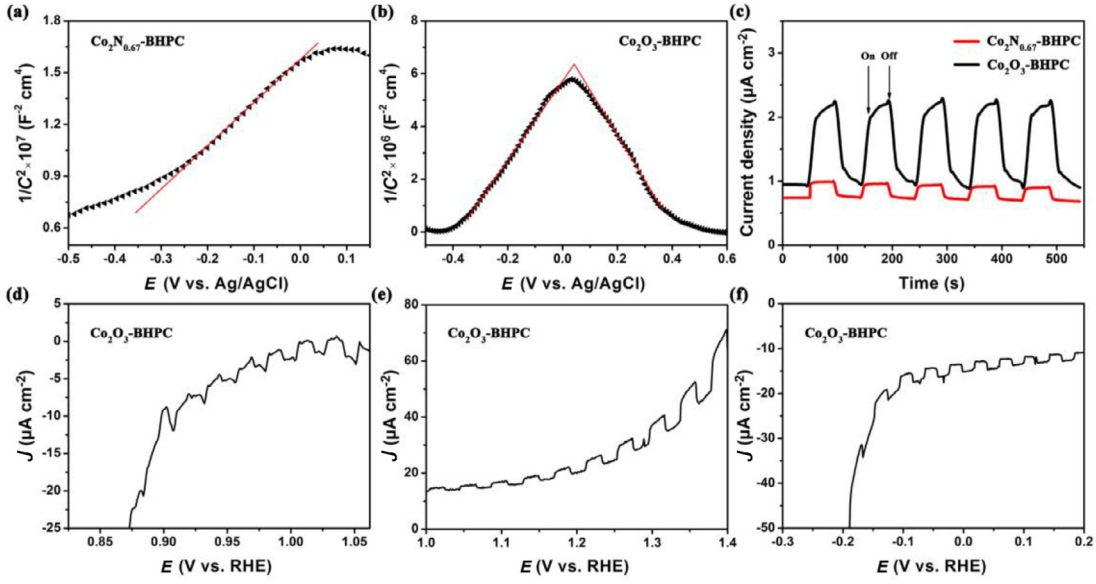

Fig. 6. Mott-Schottky curves of (a) $Co_2N_{0.67}$-BHPC and (b) Co_2O_3-BHPC. (c) The periodic on/off photocurrent response of $Co_2N_{0.67}$-BHPC and Co_2O_3-BHPC at 1.2 V bias potential vs. RHE. (d-f) J-V behaviors of Co_2O_3-BHPC under chopped light illumination.

band gap of 2.72 and 2.74 eV for $Co_2N_{0.67}$-BHPC and Co_2O_3-BHPC can be deduced from the Tauc curves obtained by UV–vis DRS measurements, Figs. S30 and S31. Consequently, the energy band diagram of two samples was portrayed in Fig. 7(a) [48]. In spite of the similar band gaps for $Co_2N_{0.67}$-BHPC and Co_2O_3-BHPC, the existence of the band tail state resulted from abundant oxygen vacancies exist in Co_2O_3-BHPC can be more efficiently separated photogenerated electrons and holes, other than a faster photogenerated charge carriers recombination in $Co_2N_{0.67}$-BHPC. This is also confirmed by the transient photocurrent response (Fig. 6c). Accordantly, the probable photoelectrochemical response mechanism for two catalysts is proposed, as shown in Fig. 7(b). Upon photoelectrochemical catalytic, C_3N_4 served as the host semiconductor can absorb the energy under visible-light irradiation, giving rise to the VB electrons to be excited to the CB accompanied by the photo-induced hole generated in VB of C_3N_4 simultaneously. The p-type Co_2O_3 stem from *in-situ* preparation manner closely interacted with the N-doped carbon containing the phase of C_3N_4, resulting in numerous p-n junction formed within Co_2O_3-BHPC. Precisely because of this point, photogenerated holes accumulated on VB of C_3N_4 swiftly transfer to Co_2O_3 (as an oxidation cocatalyst) [49]. That is to say oxidation cocatalyst Co_2O_3 is able to trap the photogenerated holes. In the meantime, the photogenerated electrons emerging from the CB of host semiconductor C_3N_4 are immediately transferred to N-doped carbon (as a reduction cocatalyst) in Co_2O_3-BHPC [49,50]. As for $Co_2N_{0.67}$-BHPC, only reduction cocatalysts exist in material, which are *in situ* formed transition metal nitride ($Co_2N_{0.67}$) nanocrystals and N-doped carbon [51].

Hence, photogenerated electrons on the CB of host semiconductor C_3N_4 also can be efficiently transferred to $Co_2N_{0.67}$ and N-doped

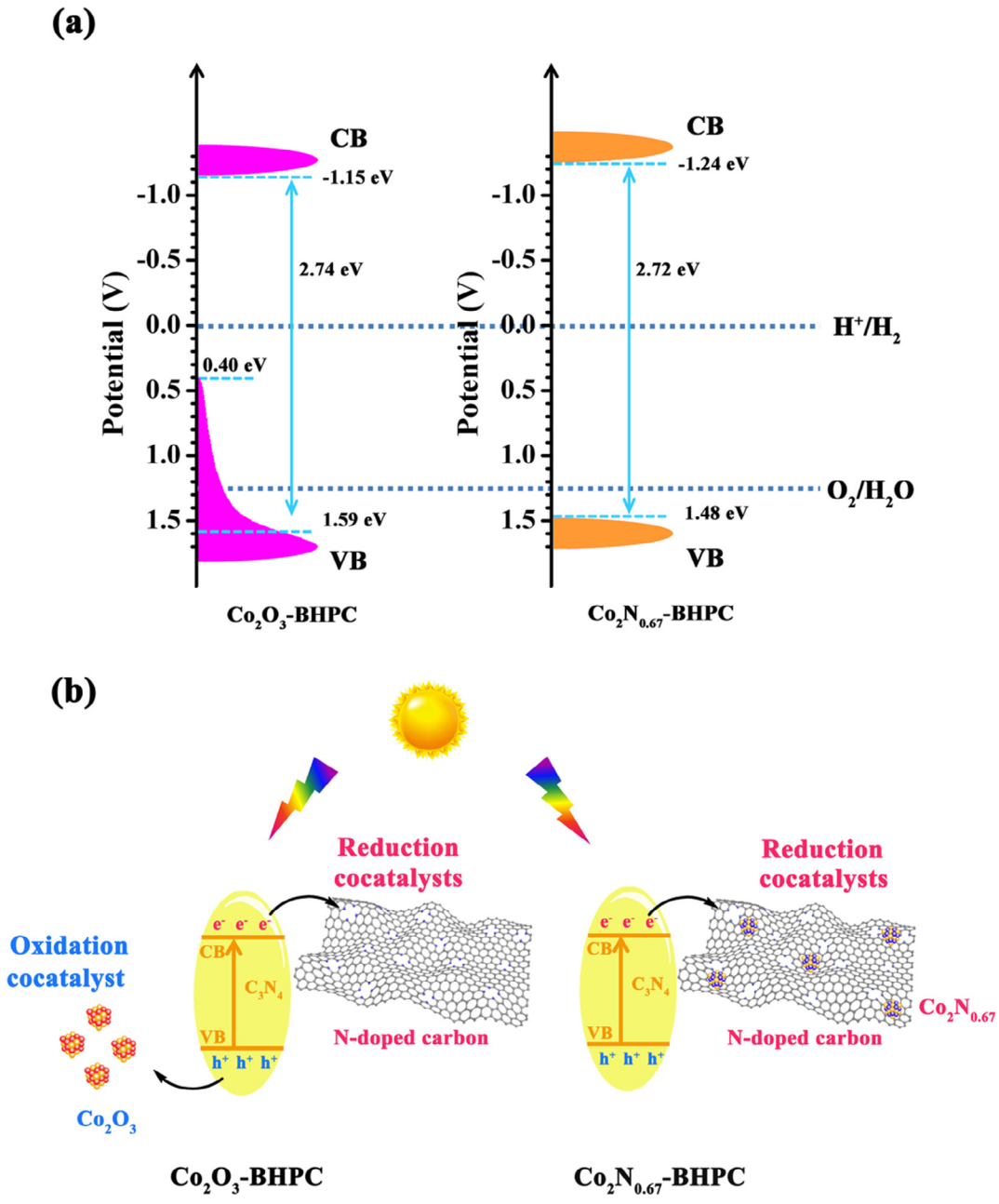

Fig. 7. (a) The Proposed energy band diagrams of Co_2O_3-BHPC and $Co_2N_{0.67}$-BHPC. (b) Schematic illustration of the mechanism for photoelectrochemical reaction.

carbon. Abundantly uncaptured or untransferred holes accumulated on the VB of C_3N_4 still accelerates the recombination of photogenerated electron-hole pairs to some extent in spite of transferred photo-induced electrons from the CB of C_3N_4 to reduction cocatalysts [52]. In brief, in Co_2O_3-BHPC obtained by *in situ* calcination, photogenerated electron-hole pairs can be effectively accelerate the separation caused by the synergistic effect between oxidation and reduction dual cocatalysts (as shown in the above transient photocurrent measurements), bringing along the significantly enhanced performance of the photoelectrochemical catalysis. As for $Co_2N_{0.67}$-BHPC, the lack of oxidation cocatalyst will be incapable of efficiently consuming the photogenerated holes, leading to distinct recombination of photogenerated electron-hole pairs in comparison with Co_2O_3-BHPC. As a result, the Co_2O_3-BHPC exhibits the significantly enhanced photoelectrochemical catalytic performance, by contrast, $Co_2N_{0.67}$-BHPC displays a more stable one.

4. Conclusions

To summarize, isotype and anisotype heterojunction materials were fabricated through protective and unprotected strategy for macrocyclic central Co-N_4, which is utilize the *in situ* π-π interaction of similar macrocyclic compounds. Heterostructure engineering serves as an effective mean to modulate the electronic and surface properties of catalysts. As expected, isotype heterojunction $Co_2N_{0.67}$-BHPC decorated with $Co_2N_{0.67}$ nanocrystals supported on N-doped carbon matrix, as an efficient catalyst for ORR, OER and HER, presented the preeminent performance and outstanding stability, benefiting from the high conductivity and stability of cobalt nitrides, larger surface area, abundant defects and rapid charge transfer at heterojunction interface. The $Co_2N_{0.67}$-BHPC derived Zn-air battery also exhibits higher maximum power density and charge–discharge cycle stability. In addition, anisotype heterojunction Co_2O_3-BHPC can boost the electrocatalytic activity in photoelectrochemical catalytic measurements. Based on it, the suitable energy band structures of two catalysts combined with the presence of reduction and/or oxidation cocatalysts are expected to response the photoelectrochemical catalytic enhancement and stability. This work provides a new and simple method to construct the biomass derived isotype and anisotype heterojunction for multifunctional electrocatalytic reaction and offers the research foundation of photoelectrochemical multifunctional catalysis.

Declaration of Competing Interest

The authors declare that they have no known competing financial interests or personal relationships that could have appeared to influence the work reported in this paper.

Acknowledgments

This work was financially supported by the National Natural Science Foundation of China (21771192), and Major Program of Shandong Province Natural Science Foundation (ZR2017ZB0315), Program for Taishan Scholar of Shandong Province (ts201712019), the Fundamental Research Funds for the Central Universities (19CX05001A, 18CX02053A), and Qingdao Applied Basic Research Project (19-6-2-20-cg), Yankuang Group 2019 Science and Technology Program.

Appendix A. Supplementary data

Supplementary data to this article can be found online at https://doi.org/10.1016/j.jechem.2020.06.040.

References

[1] (a) R. Paul, L. Zhu, H. Chen, J. Qu, L. Dai, Adv. Mater. 31 (2019) 1806403;
(b) Z. Yang, C. Zhao, Y. Qu, H. Zhou, F. Zhou, J. Wang, Y. Wu, Y. Li, Adv. Mater. 31 (2019) 1808043;
(c) X. Liu, L. Wang, P. Yu, C. Tian, F. Sun, J. Ma, W. Li, H. Fu, Angew. Chem. Int. Ed. 49 (2018) 16166–16170;
(d) X. Li, H. Lei, J. Liu, X. Zhao, S. Ding, Z. Zhang, X. Tao, W. Zhang, W. Wang, X. Zheng, R. Cao, Angew. Chem. Int. Ed. 57 (2018) 15070–15075.
[2] (a) J. Meng, H. Lei, X. Li, J. Qi, W. Zhang, R. Cao, ACS Catal. 9 (2019) 4551–4560;
(b) Z. Xing, Y.-P. Deng, S. Sy, G. Tan, A. Li, J. Li, Y. Niu, N. Li, D. Su, J. Lu, Z. Chen, Nano Energy 65 (2019) 104051;
(c) W. Liu, C. Wang, L. Zhang, H. Pan, W. Liu, J. Chen, D. Yang, Y. Xiang, K. Wang, J. Jiang, X. Yao, J. Mater. Chem. A 7 (2019) 3112–3119;
(d) L. Xie, X. Li, B. Wang, J. Meng, H. Lei, W. Zhang, R. Cao, Angew. Chem. Int. Ed. 58 (2019) 18883–18887.
[3] (a) K. Yuan, D.F. Lützenkirchen-Hecht, L. Li, L. Shuai, Y. Li, R. Cao, M. Qiu, X. Zhuang, Y. Chen, M.K.H. Leung, U. Scherf, J. Am. Chem. Soc. 142 (2020) 2404–2412;
(b) H.-F. Wang, C. Tang, Q. Zhang, Adv. Funct. Mater. 28 (2018) 1803329;
(c) X. Guo, N. Wang, X. Li, Z. Zhang, J. Zhao, W. Ren, S. Ding, G. Xu, J. Li, U.-P. Apfel, W. Zhang, R. Cao, Angew. Chem. Int. Ed. (2020), https://doi.org/10.1002/anie.202002311.
[4] L. Tao, Y. Wang, Y. Zhou, N. Zhang, Y. Zhang, Y. Wu, Y. Wang, R. Chen, S. Wang, Adv. Energy Mater. 9 (2019) 1901227.
[5] (a) C. Tang, L. Zhong, B. Zhang, H.-F. Wang, Q. Zhang, Adv. Mater. 30 (2018) 1705110;
(b) H. Yan, Y. Xie, A. Wu, Z. Cai, L. Wang, C. Tian, X. Zhang, H. Fu, Adv. Mater. 31 (2019) 1901174;
(c) Y. Liu, X. Luo, C. Zhou, S. Du, D. Zhen, B. Chen, J. Li, Q. Wu, Y. Iru, D. Chen, Appl. Catal. B 260 (2020) 118197;
(d) P. Yu, L. Wang, F. Sun, Y. Xie, X. Liu, J. Ma, X. Wang, C. Tian, J. Li, H. Fu, Adv. Mater. 31 (2019) 1901666.
[6] (a) S. Song, W. Li, Y.-P. Deng, Y. Ruan, Y. Zhang, X. Qin, Z. Chen, Nano Energy 67 (2020) 104208;
(b) H. Li, X. Li, H. Lei, G. Zhou, W. Zhang, R. Cao, ChemSusChem 12 (2019) 801–806.
[7] Y. Shao, J.-P. Dodelet, G. Wu, P. Zelenay, Adv. Mater. 31 (2019) 1807615.
[8] (a) D. Banham, S. Ye, K. Pei, J. Ozaki, T. Kishimoto, Y. Imashiro, J. Power Sour. 285 (2015) 334–348;
(b) U. Martinez, S.K. Babu, E.F. Holby, P. Zelenay, Curr. Opin. Electrochem. 9 (2018) 224–232;
(c) H. Singh, S. Zhuang, B. Ingis, B.B. Nunna, E.S. Lee, Carbon 151 (2019) 160–174.
[9] W.Y. Noh, J.H. Lee, J.S. Lee, Appl. Catal. B 268 (2020) 118415.
[10] H. Zou, G. Li, L. Duan, Z. Kou, J. Wang, Appl. Catal. B 259 (2019) 118100.
[11] W. Yuan, S. Wang, Y. Ma, Y. Qiu, Y. An, L. Cheng, ACS Energy Lett. 5 (2020) 692–700.
[12] (a) W. Ni, A. Krammer, C.-S. Hsu, H.M. Chen, A. Schüler, X. Hu, Angew. Chem. Int. Ed. 58 (2019) 7445–7449;
(b) F. Song, W. Li, J. Yang, G. Han, T. Yan, X. Liu, Y. Rao, P. Liao, Z. Cao, Y. Sun, ACS Energy Lett. 4 (2019) 1594–1601;
(c) B.K. Kang, S.Y. Im, J. Lee, S.H. Kwag, S.B. Kwon, S. Tiruneh, M.-J. Kim, J.H. Kim, W.S. Yang, B. Lim, D.H. Yoon, Nano Res. 12 (2019) 1605–1611.
[13] Y. Guo, P. Yuan, J. Zhang, H. Xia, F. Cheng, M. Zhou, J. Li, Y. Qiao, S. Mu, Q. Xu, Adv. Funct. Mater. 28 (2018) 1805641.
[14] J. Lv, S.C. Abbas, Y. Huang, Q. Liu, M. Wu, Y. Wang, L. Dai, Nano Energy 43 (2018) 130–137.
[15] (a) H. Zhu, X. Wang, F. Yang, X. Yang, Adv. Mater. 23 (2011) 2745–2748;
(b) Z. Wang, D. Shen, C. Wu, S. Gu, Green Chem. 20 (2018) 5031–5057.
[16] (a) M. Borghei, J. Lehtonen, L. Liu, O.J. Rojas, Adv. Mater. 30 (2018) 1703691;
(b) J. Niu, R. Shao, M. Liu, Y. Zan, M. Dou, J. Liu, Z. Zhang, Y. Huang, F. Wang, Adv. Funct. Mater. 29 (2019) 1905095;
(c) R. Paul, L. Zhu, H. Chen, J. Qu, L. Dai, Adv. Mater. 31 (2019) 1806403.
[17] (a) Z. Zhang, S. Yang, H. Li, Y. Zan, X. Li, Y. Zhu, M. Dou, F. Wang, Adv. Mater. 31 (2019) 1805718;
(b) Y. Zhao, X. Li, X. Jia, S. Gao, Nano Energy 58 (2019) 384–391;
(c) X. Lv, Y. Chen, Y. Wu, H. Wang, X. Wang, C. Wei, Z. Xiao, G. Yang, J. Jiang, J. Mater. Chem. A 7 (2019) 27089–27098.
[18] (a) W. Liu, J. Ji, X. Yan, W. Liu, Y.-C. Huang, K. Wang, P. Jin, X. Yao, J. Jiang, J. Mater. Chem. A 8 (2020) 5255–5262;
(b) C. Zhang, H. Yang, D. Zhong, Y. Xu, Y. Wang, Q. Yuan, Z. Liang, B. Wang, W. Zhang, H. Zheng, T. Cheng, R. Cao, J. Mater. Chem. A (2020), https://doi.org/10.1039/D0TA00962H;
(c) X. Lv, Y. Chen, Y. Wu, H. Wang, X. Wang, C. Wei, Z. Xiao, G. Yang, J. Jiang, J. Mater. Chem. A 7 (2019) 27089–27098.
[19] C. Hu, L. Dai, Angew. Chem. Int. Ed. 55 (2016) 11736–11758.
[20] T. Liu, M. Li, Z. Su, X. Bo, W. Guan, M. Zhou, ACS Appl. Nano Mater. 1 (2018) 4461–4473.
[21] T. Xu, R. Zou, X. Lei, X. Qi, Q. Wu, W. Yao, Q. Xu, Appl. Catal. B 245 (2019) 662–671.
[22] J. Zhang, M. Zhang, Y. Zeng, J. Chen, L. Qiu, H. Zhou, C. Sun, Y. Yu, C. Zhu, Z. Zhu, Small 15 (2019) 1900307.
[23] Y. Zhou, Y. Yang, R. Wang, X. Wang, X. Zhang, L. Qiang, W. Wang, Q. Wang, Z. Hu, J. Mater. Chem. A 6 (2018) 19038–19046.

[24] (a) H. Zeng, W. Wang, J. Li, J. Luo, S. Chen, ACS Appl. Mater. Interfaces 10 (2018) 8721–8729;
(b) C. Zhu, M. Takata, Y. Aoki, H. Habazaki, Chem. Eng. J. 350 (2018) 278–289.
[25] S. Gao, H. Liu, K. Geng, X. Wei, Nano Energy 12 (2015) 785–793.
[26] X. Wan, X. Liu, Y. Li, R. Yu, L. Zheng, W. Yan, H. Wang, M. Xu, J. Shui, Nat. Catal. 2 (2019) 259–268.
[27] (a) H. Wang, D. Mao, J. Qi, Q. Zhang, X. Ma, S. Song, L. Gu, R. Yu, D. Wang, Adv. Funct. Mater. 29 (2019) 1806588;
(b) Y. Liu, F. Zhan, B. Wang, B. Xie, Q. Sun, H. Jiang, J. Li, X. Sun, ACS Appl. Mater. Interfaces 11 (2019) 21526–21535.
[28] L. Wang, K. Liang, L. Deng, Y.-N. Liu, Appl. Catal. B 246 (2019) 89–99.
[29] (a) Q. Lu, J. Yu, X. Zou, K. Liao, P. Tan, W. Zhou, M. Ni, Z. Shao, Adv. Funct. Mater. 29 (2019) 1904481;
(b) P. Tan, B. Chen, H. Xu, W. Cai, W. He, M. Ni, Appl. Catal. B 241 (2019) 104–112.
[30] S. Dou, L. Tao, J. Huo, S. Wang, L. Dai, Energy Environ. Sci. 9 (2016) 1320–1326.
[31] X. Yan, Y. Jia, X. Yao, Chem. Soc. Rev. 47 (2018) 7628–7658.
[32] (a) D. Guo, R. Shibuya, C. Akiba, S. Saji, T. Kondo, J. Nakamura, Science 351 (2016) 361–365;
(b) H. Jiang, J. Gu, X. Zheng, M. Liu, X. Qiu, L. Wang, W. Li, Z. Chen, X. Ji, J. Li, Energy Environ. Sci. 12 (2019) 322–333.
[33] (a) H. Han, Z. Bai, T. Zhang, X. Wang, X. Yang, X. Ma, Y. Zhang, L. Yang, J. Lu, Nano Energy 56 (2019) 724–732;
(b) T. Najam, S.S.A. Shah, W. Ding, J. Jiang, L. Jia, W. Yao, L. Li, Z. Wei, Angew. Chem. Int. Ed. 57 (2018) 15101–15106;
(c) X.F. Lu, Y. Chen, S. Wang, S. Gao, X.W. Lou, Adv. Mater. 31 (2019) 1902339.
[34] (a) M. Kuang, P. Han, L. Huang, N. Cao, L. Qian, G. Zheng, Adv. Funct. Mater. 28 (2018) 1804886;
(b) Z. Li, Y. Zhang, Y. Feng, C.-Q. Cheng, K.-W. Qiu, C.-K. Dong, H. Liu, X.-W. Du, Adv. Funct. Mater. 29 (2019) 1903444;
(c) D. Ji, L. Fan, L. Tao, Y. Sun, M. Li, G. Yang, T.Q. Tran, S. Ramakrishna, S. Guo, Angew. Chem. Int. Ed. 58 (2019) 13840–13844.
[35] Y. Wang, R. Zhang, J. Chen, H. Wu, S. Lu, K. Wang, H. Li, C.J. Harris, K. Xi, R.V. Kumar, S. Ding, Adv. Energy Mater. 9 (2019) 1900953.
[36] Y. Zhao, X. Li, X. Jia, S. Gao, Nano Energy 58 (2019) 384–391.
[37] (a) J. Chen, X. Yuan, F. Lyu, Q. Zhong, H. Hu, Q. Pan, Q. Zhang, J. Mater. Chem. A 7 (2019) 1281–1286;
(b) Q. Jin, B. Ren, J. Chen, H. Cui, C. Wang, Appl. Catal. B 256 (2019) 117887;
(c) M. Leng, X. Huang, W. Xiao, J. Ding, B. Liu, Y. Du, J. Xue, Nano Energy 33 (2017) 445–452.
[38] (a) Y. Lou, J. Liu, M. Liu, F. Wang, ACS Catal. 10 (2020) 2443–2451;
(b) X. Dong, H. Yan, Y. Jiao, D. Guo, A. Wu, G. Yang, X. Shi, C. Tian, H. Fu, J. Mater. Chem. A 7 (2019) 15823–15830.
[39] W. Jiao, C. Chen, W. You, G. Chen, S. Xue, J. Zhang, J. Liu, Y. Feng, P. Wang, Y. Wang, H. Wen, R. Che, Appl. Catal. B 262 (2020) 118298.
[40] X. Gao, Y. Chen, T. Sun, J. Huang, W. Zhang, Q. Wang, R. Cao, Energy Environ. Sci. 13 (2020) 174–182.
[41] (a) J. Wang, F. Xu, H. Jin, Y. Chen, Y. Wang, Adv. Mater. 29 (2017) 1605838;
(b) C. Lei, Y. Wang, Y. Hou, P. Liu, J. Yang, T. Zhang, X. Zhuang, M. Chen, B. Yang, L. Lei, C. Yuan, M. Qiu, X. Feng, Energy Environ. Sci. 12 (2019) 149–156;
(c) T. Ouyang, Y.-Q. Ye, C.-Y. Wu, K. Xiao, Z.-Q. Liu, Angew. Chem. Int. Ed. 58 (2019) 4923–4928.
[42] (a) X. Zhou, S. Wu, C. Li, F. Yan, H. Bai, B. Shen, H. Zeng, J. Zhai, Nano Energy 66 (2019) 104127;
(b) X.-J. Wen, C.-G. Niu, L. Zhang, C. Liang, G.-M. Zeng, Appl. Catal. B 221 (2018) 701–714;
(c) R. Jiang, X. Chen, J. Deng, T. Wang, K. Wang, Y. Chen, J. Jiang, J. Energy Chem. 47 (2020) 79–85.
[43] (a) D. Liu, D. Chen, N. Li, Q. Xu, H. Li, J. He, J. Lu, Small 15 (2019) 1902291;
(b) F. Meng, J. Li, S.K. Cushing, M. Zhi, N. Wu, J. Am. Chem. Soc. 135 (2013) 10286–10289.
[44] Y.-Y. Han, X.-L. Lu, S.-F. Tang, X.-P. Yin, Z.-W. Wei, T.-B. Lu, Adv. Energy Mater. 8 (2018) 1702992.
[45] S. Hua, D. Qu, L. An, W. Jiang, Y. Wen, X. Wang, Z. Sun, Appl. Catal. B 240 (2019) 253–261.
[46] J. Cai, A. Cao, J. Huang, W. Jin, J. Zhang, Z. Jiang, X. Li, Appl. Catal. B 267 (2020) 118378.
[47] Z. Lin, C. Du, B. Yan, C. Wang, G. Yang, Nat. commun. 9 (2018) 4036.
[48] A. Hezam, K. Namratha, Q.A. Drmosh, D. Ponnamma, A.M.N. Saeed, V. Ganesh, B. Neppolian, K. Byrappa, J. Mater. Chem. A 6 (2018) 21379–21388.
[49] A. Meng, L. Zhang, B. Cheng, J. Yu, Adv. Mater. 31 (2019) 1807660.
[50] Q. Liu, C. Zeng, Z. Xie, L. Ai, Y. Liu, Q. Zhou, J. Jiang, H. Sun, S. Wang, Appl. Catal. B 254 (2019) 443–451.
[51] (a) H. Chen, D. Jiang, Z. Sun, R.M. Irfan, L. Zhang, P. Du, Catal. Sci. Technol. 7 (2017) 1515–1522;
(b) L. Li, J. Yi, X. Zhu, M. Zhou, S. Zhang, X. She, Z. Chen, H.-M. Li, H. Xu, ACS Sustain. Chem. Eng. 8 (2020) 884–892;
(c) R. Mu, Y. Ao, T. Wu, C. Wang, P. Wang, J. Alloys Compd. 812 (2020) 151990.
[52] Y. Wei, G. Cheng, J. Xiong, J. Zhu, Y. Gan, M. Zhang, Z. Li, S. Dou, J. Energy Chem. 32 (2019) 45–56.